Taylor & Francis
Taylor & Francis Group

Check for updates

Micro-computed tomography based experimental investigation of micro- and macro-mechanical response of particulate composites with void growth

Katherine Ramos and Karel Matouš

Department of Aerospace and Mechanical Engineering, Center for Shock Wave-processing of Advanced Reactive Materials, University of Notre Dame, Notre Dame, IN, USA

ABSTRACT

In this work, we develop an image-based material testing approach using micro-computed tomography to understand the influence of microstructure and local damage phenomenon on the effective mechanical response of rubber-glass bead composites. Furthermore, a nondestructive, three-dimensional image-based analysis protocol which provides high fidelity of sample testing and data assessment has been established. An investigation was performed on various compositions of silicone rubber reinforced with silica particles. *In situ* compression experiments were used to study how the microscale damage (void creation from debonding) develops and evolves in the context of four primary studies: (i) effect of particle volume fraction, (ii) effect of particle diameter, (iii) local damage phenomena and its evolution (incremental loading/ unloading), and (iv) effect of surface treatments on bonding characteristics. A detailed statistical analysis of the evolution of structural features through robust image processing strategies at various stages of loading was conducted. The rich data analysis collected from the experimental studies offers an understanding of the complex phenomena attributing to the material's macro and microscopic response to loading. Altogether, this framework results in the development of microstructure-statistics-property relations. Furthermore, the mechanical and morphological response of non-linear viscoelastic materials subjected to uniaxial compression is investigated.

1. Introduction

Exploiting material performance of multi-functional materials is essential in a variety of scientific disciplines and industrial applications [1–4]. These intricate materials require detailed analysis in order to understand and utilise the unique properties that arise from their inherent heterogeneity and morphology.

CONTACT Karel Matouš ✉ kmatous@nd.edu; kramos5@nd.edu 🖂 Department of Aerospace and Mechanical Engineering, Center for Shock Wave-processing of Advanced Reactive Materials, University of Notre Dame, Notre Dame, IN 46556, USA

However, the underlying mechanics at different length scales which govern material behaviour is yet to be fully understood and with major advancements in computing and scientific equipment, this missing gap can be filled [5,6]. Traditionally, material development has followed a conventional threefold platform consisting of experimentation, computation, and constitutive theory (used independently) to understand material's behaviour [7]. This unidisciplinary approach is a timely and costly one, adding a major limitation to material innovation. As such, there is a need for a multi-disciplinary approach in material design to reduce the product development to market time cycle and is called the *Integrated Computational Materials Engineering* (ICME) paradigm [6,8,9]. ICME consolidates the threefold platform into one framework. One of the components is a methodology that challenges the traditionally material design approach to exploit the use of experimental data at multiple length scales and its ability to guide computations (data guided design). As such, we present an image-based material testing approach to augment the role of experimental data and establish image-based protocols for nondestructive analysis of reinforced polymers.

It is known that understanding the macroscopic behaviour of heterogeneous systems is dependent on the accurate characterisation of the material's microstructure [10–12]. Specifically, statistical characterisation has greatly aided the understanding of microstructure and its impact on material performance [13–15]. For decades, imaging tools such as the Transmission Electron Microscope (TEM), and Scanning Electron Microscope (SEM) offered unprecedented high-resolution optical access. In addition, the Focused Ion Beam (FIB) became suitable for sample preparation for TEM/SEM analysis [16] and served as a stand-alone instrument for micromachining of materials [17]. These tools are used to image materials including silicates [18], carbonates [19], metals alloys [20], ceramic materials [21], diamond [22], thermal interface materials [23], and high energy ball milled composites [24]. These techniques, however, are often destructive approaches for material testing. They require intricate sample preparation and impose sample size restrictions. Lastly, they are limited to surface analysis and offer no mechanical *in situ* testing capabilities.

On the contrary, noninvasive imaging techniques include Magnetic Resonance Imaging (MRI) and Computed Tomography (CT). The MRI technique is most suited for biological systems and has a very extensive acquisition time associated with it [25]. Contrastingly, tomography techniques which use X-rays are far more suited for non-biological systems while offering the same internal high-resolution examination with mechanical testing capabilities [26]. X-ray micro-computed tomography (micro-CT) and synchrotron micro-CT, have become popular methods in the materials science community for nondestructive *in situ* analysis and characterisation of the internal microstructure of complex materials [27–33]. These techniques have been implemented to facilitate morphological characterisation of material systems such as propellants [34],

glass beads [13], porous foam structures [35], metal foams [36–38] and particulate composites [14] to name a few.

Understanding the mechanical behaviour that arises from the heterogeneity at different length scales of complex material systems has been a long-standing endeavour in the materials science community. Thus, Hounsfield's development of the first commercial computed tomography system in the 1970s, used for medical imaging, was an indispensable achievement for material characterisation techniques [39]. In time, computed tomography was being used to study damage due to the processing of materials, response to deformation, damage mechanisms, and much more [40–43]. However, in all of these works, the materials were examined post external stimuli, and thus, unable to capture critical features of the material response. Guvenilir et al. [44], one of the earliest adopters of *in situ* micro-CT experiments, studied crack closure in an Aluminium-Lithium alloy. Since then, many advancements in this characterisation technique and modelling strategies have evolved and resulted in the integration of the two. These developments have led to the leveraging of 3D data acquired from *in situ* tomographic scans to quantify comparisons between modelling results and experiments [45–51]. Nguyen et al. [52] presented direct comparisons of the modelling of microcracking initiation and propagation in plaster and concrete materials and X-ray micro-CT images collected during *in situ* testing for a limited number of samples and modest volumes of the tomographic data.

Recently, characterisation techniques capable of resolving microstructural features using tomographic images such as Particle Tracking method [53] and Digital Volume Correlation (DVC) [54] have allowed for the tracking of displacement of individual features and have yet to be fully explored [55–59]. While the combination of real 3D tomographic data (used to realise a material's microstructure) and modelling frameworks have been used more frequent [14,60–65], limiting material sampling, absence of detailed image processing steps, and restrained tomographic data sizes leave room for error in repeatability, consistency, and accuracy. Furthermore, given the intricate nature of a material's morphology robust qualitative and quantitative *in situ* analysis is necessary to better understand the driving mechanisms involved when mechanically loading the system.

In this work, we utilise the micro-CT technique to investigate the effect of the microstructure on the damage (void creation from debonding) nucleation and evolution in rubber-glass bead composites in the context of four studies: (i) effect of particle volume fraction, (ii) effect of particle diameter, (iii) local damage phenomena and it's evolution (incremental loading/unloading), and (iv) effect of surface treatments on bonding characteristics. We select the rubber-glass composition, i.e. a model system, to mimic materials such as solid rocket propellants [66,67]. Moreover, our model system allows for rigorous experimental procedure development and assessment, which would be difficult with added material complexity. We assess repeatability and consistency, for each of these studies, by sampling 3× and utilise the large data sets acquired

for all statistical calculations. We directly examine the material's microstructure before and during uniaxial compression loading to discern multiscale linking and evolution of fields when assessing the damage. Void evolution under compressive loads is important for safety assessment in numerous applications, for example, when dealing with high-explosives [68,69]. In particular, when the combustion front reaches the voided regions, the burning characteristics can change and the material can transition to detonation with a catastrophic consequence. Thus, studying the void evolution under compression is an important topic. Additionally, we use image analysis tools and develop protocols to quantify damage in the composite through statistical calculations of void volume fractions and void size distributions. Altogether, this leads to the development of microstructure-statistics-property relations [14]. Furthermore, we improve the understanding between microstructures and void nucleation/evolution together with the macroscopic response of particulate composites subjected to uniaxial compression loading.

The remainder of this paper is organised as follows. In Section 2, we discuss the material formulation of rubber-glass bead composites. In Section 3, a thorough description of experimental procedures which includes data acquisition, post-processing, machine accuracy and material consistency, and image processing is given. In Section 4, we examine the four material studies through a qualitative and quantitative analysis of the amount of microscale damage in the composites created in Section 2. Lastly, a few conclusions are made in Section 5.

2. Material formulation

We develop and implement a material formulation protocol to prepare composite samples in a consistent manner. This protocol is similar to methods presented in [13,14]. In this work, a composite system consisting of a silicone rubber binder (Polytek PlastSil 73–40) and (Ballotini) silica glass beads from Jencons, a VWR Company (UK) is used. The methodology is as follows: (I) To ensure uniformity and sphericity of particles, we remove the non-spherical particles by rolling them down on an inclined plane and remove any beads that did not roll. (II) Following this purification step, we weigh the amount of each constituent (e.g. glass beads, parts A and B of the polymer) using a high precision scale with 0.001 g accuracy. (III) We mix the constituents in a large bowl by stirring them manually until fully blended (a 45 minute working time is considered for the remainder of this procedure). (IV) We place the mixture into a Shel Lab SVAC1 Vacuum Oven where a Welch-ILMVAC vacuum pump is used to pull a high vacuum (∼29 in. Hg) to allow degassing for 15 minutes. (V) We remove the mixture from the vacuum oven and gently pour into a lightly lubricated (Polytek Pol-Ease 2500 Release Agent) mould containing a total of 10 cylindrical samples. (VI) We place the filled mould back into the

vacuum oven and keep it under full vacuum for an additional 15 minutes to degas the samples. (VII) The samples all allowed to cure for 48 hours at room temperature prior to removing from the mould.

3. Experimental procedures

We select three samples for mechanical testing at random from each batch and test them using a Skyscan 1172 micro-CT scanner. This scanner has the ability to capture *in situ* spatial features of ~5 microns as well as provide overall load displacement profiles. An individual sample is scanned at a 10.81 μm/pixel resolution inside the material testing stage (MTS) chamber. The average particle diameter, of the standard sample, is 261 μm. With a resolution of 10.81 μm/pixel, this is ~24 voxels (3D pixel) in diameter of a particle and approximately 7,531 voxels representing one particle volume. The composite sample has a diameter and height of ~10 mm (925 pixels), which corresponds to 6.22×10^8 voxels. This is approximately 1.64 times the number of voxels used in [14]. Therefore, a 10.81 μm/pixel resolution is considered a good resolution for the statistical characterisation performed in this work.

To perform the mechanical testing, a Teflon film is used between the compression plates and the specimens to limit the effect of friction when specimens are loaded. A relaxation experiment concluded a relaxation time of 24 hours is sufficient for all experiments before initialising a tomographic scan after compression. This relaxation is required due to the viscoelastic response observed in the polymer (see Figure 1(b)).

The *in situ* experimental protocol is summarised as follows: (i) An initial micro-CT scan of the composite is taken at an unloaded (zero load) state. (ii) The sample is loaded to a predefined load and relaxed. (iii) A second micro-CT scan, with the same resolution at the loaded state (predefined load), is
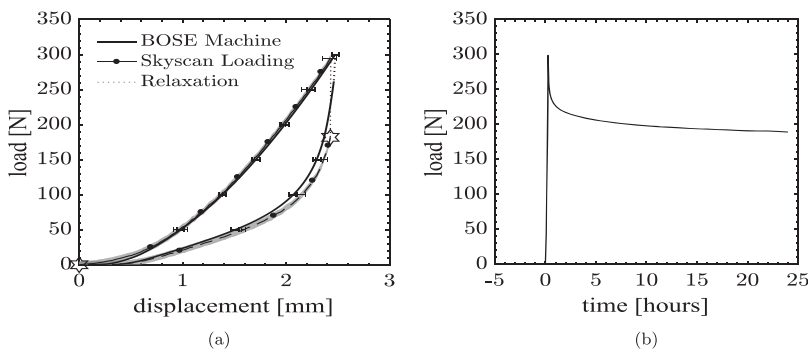

Figure 1. (a) The loading curve for the standard rubber-silica composite depicts the experimental protocol where the open stars serve as micro-CT acquisition markers (i.e. where the 3D scans were taken, at initial and loaded states) and (b) the relaxation study demonstrates a load relaxation plateau used to determine the relaxation period for experimental testing.

taken. The force-displacement curve in Figure 1(a) is representative of the described experimental protocol where the horizontal error bars represent the minimum and maximum displacement (range of displacements) seen among the three samples tested. The shaded grey area depicts the accuracy of the load cell (±4.4 N) of the MTS. Note, the force-displacement curve can be easily transformed into an engineering stress-strain curve given the sample's surface area and height.

Given the load cell inaccuracies (e.g. surface not being perfectly parallel), setting the initial (0 displacement/ 0 load) state requires careful consideration. Therefore, the force-displacement data acquisition and correction steps are detailed in Procedure I:

Procedure I: Obtaining force-displacement data using *in situ* MTS

Step 1: Place specimen in a chamber under no load.
Step 2: Obtain a projection image of the compression plates starting position to quantify original configuration.
Step 3: Compress specimen to predefined load.
Step 4: Obtain projection image at maximum displacement and unload the specimen.
Step 5: Post-process collected acquisition data.

The projection images are used to determine the origin of the loading curve and capture the initial small load regime where inaccuracies are high. This is done by first optically measuring the original sample height (l_o) and the final sample height (l_f) from the projection images. Then, the difference, (u), is defined as

$$u = l_f - (l_o + \delta_{MAX}),\qquad(1)$$

where δ_{MAX} is the acquired maximum displacement measured using the MTS. Next, u is subtracted from the full displacement profile. It should be noted, the force-displacement data is considered reliable when increasing monotonically and outside of the initial range of uncertainty.

In order to provide a comparison to the mechanical response of the composites, the pure rubber response is presented in this section. The results from the compression testing shown in Figure 2 indicate that the rubber has a nonlinear viscoelastic response. Within the figure, the horizontal error bars represent the uncertainty associated with the repeatability of the three tests.

3.1. Machine accuracy and material consistency

In order to verify the accuracy and consistency of methodologies, the composites with a particle volume fraction, $c_p = 0.4$, are compared against a standard materials testing device (BOSE Mechanical Tester, 3300 AT, System ID 33A0022). The BOSE testing device has a confidence interval of ±0.5% of the applied load (300 N) [70]. Figure 1(a) shows good agreement between BOSE and MTS systems using our correction procedure (i.e. Procedure I).
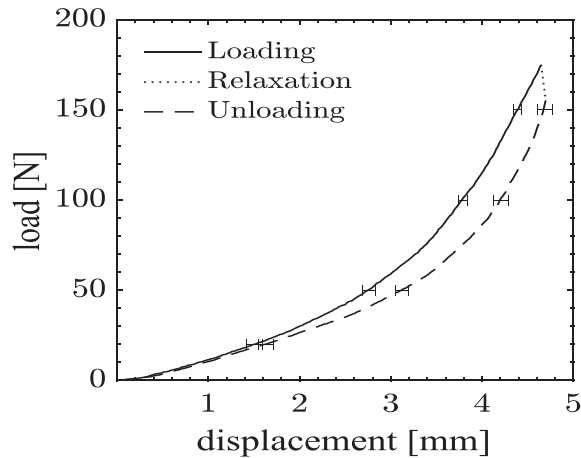
Figure 2. Averaged force displacement curve of the pure silicone rubber.

To ensure repeatability and consistency of material formulations from a physics perspective the following metrics are measured on samples from different batches. We confirm in the first metric that the force-displacement curve from a subsequent batch falls within the spread of the average loading curve of the standard sample study. Secondly, a comparison of the weights (in grams) of the two batches shows less than 0.018% difference for all samples, where the percent difference, ϵ_D, is calculated as $\epsilon_D = (W_1 - W_2)/((W_1 + W_2)/2) \times 100[\%]$. The standard deviation in weights for all samples from one batch is 0.012 and for the next batch 0.005. Lastly, using the image processing algorithms to follow, the particle volume fraction shows less than 1% difference in the mean. The experiments are therefore considered repeatable and consistent from batch to batch. The image processing algorithms are given next.

3.2. Image processing

Upon acquiring three-dimensional voxel data of initial and compressed states, image processing algorithms are used to analyze and acquire geometrical quantities of individual particles and voids. The following image processing steps are developed using *Avizo Fire* [71] along with CT Analyzer (CTAn) [72] and are similar to ones used in [14]: (I) A volume of interest (VOI) is identified for image processing. (II) An edge-preserving smoothing algorithm, Symmetric Nearest Neighbor (SNN) Filter [71], is implemented to filter out noise while preserving the data Figure 3(a). (III) A greyscale distribution, represented by a histogram Figure 3(b), is used to identify/segment the phases of interest. The greyscale values contain intensity information in the form of integers ranging between 0–255, where zero is taken to be black and 255 is taken to be white. In this distribution, the two prominent far-right peaks are related to the
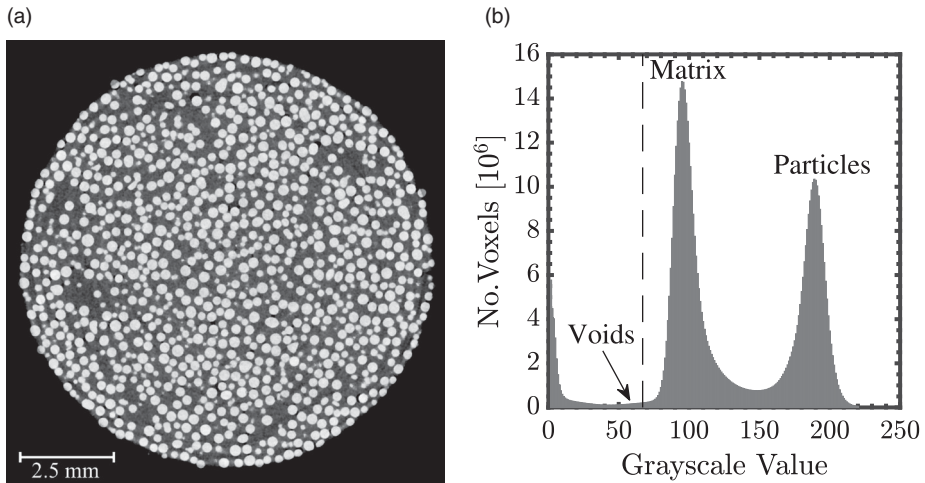
Figure 3. (a) Gray scale image after applying edge-preserving smoothing algorithm. (b) Distribution of voxel grey scale values are used for phase identification.

average greyscale values of the matrix and particles phase, respectively. The furthest left peak is black background and the lower end of the most prominent peak (close to the matrix phase peak) corresponds to the voids. (IV) The data is segmented at the cutoff (dashed line) to aid in the removal of background and promote void identification. (V) Preexisting voids within the particles (from manufacturing) are filled via a 'fill holes' algorithm. (VI) The background data is subtracted from the segmented data of interest in step IV and a new data is created. (VII) The phase of interest is selected. (VIII) An opening algorithm is applied to filter out noise and reduce artefacts Figure 4(a). (IX) A high-level combination of watershed, distance transform, and numerical reconstruction algorithms [71] are used to separate individual particles, which is achieved by
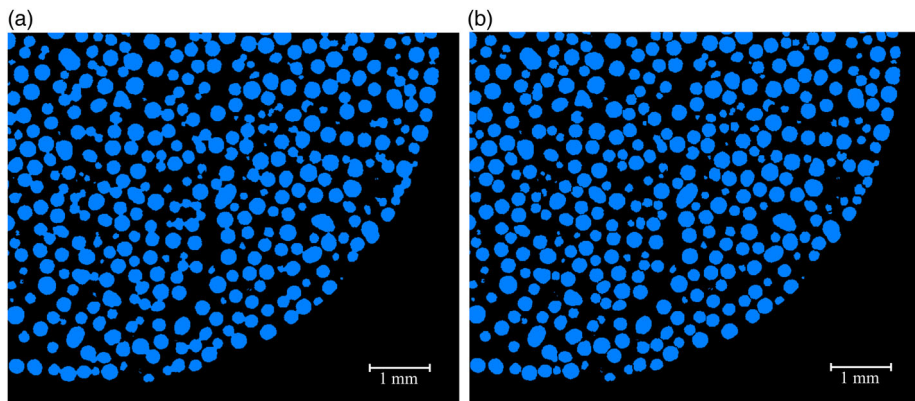

Figure 4. (a) Isolated phase (particles) prior to segmentation algorithm (watershed, distance transform, and numerical reconstruction) and (b) resulting data slice after segmentation steps.
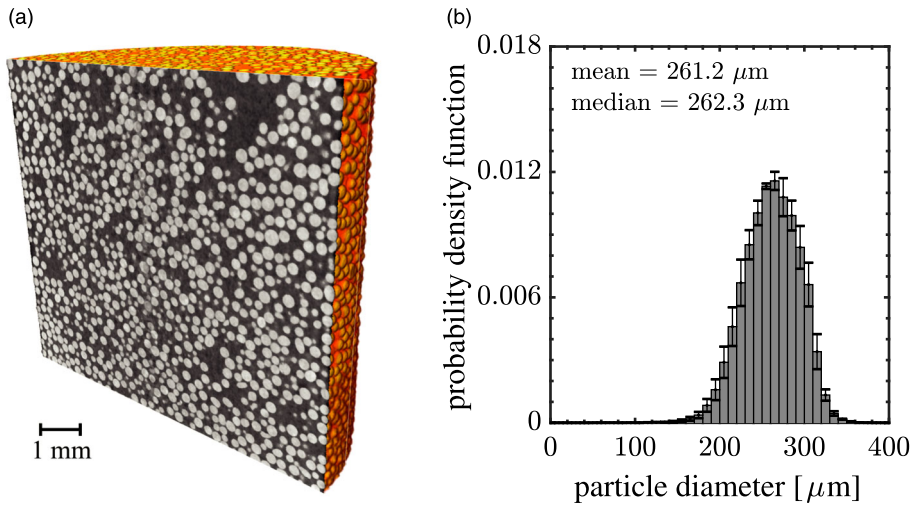
(a)

1 mm

(b)

mean = 261.2 μm
median = 262.3 μm

probability density function

particle diameter [μm]

Figure 5. (a) A three-dimensional representation of the standard sample study ($c_p = 0.4$, $d = 261\,\mu$m) and (b) the mean particle size distribution where vertical error bars represent ($\pm\,2\sigma$) from the mean value between three tested samples.

detecting the surfaces that separate the agglomerates and subtracts them Figure 4 (b). (X) Geometrical quantities of interest are calculated. Note, a border kill algorithm is implemented to remove all particles (i.e. edge artefacts) that are intersecting the border of the sample prior to analysis. Additionally, steps VIII and IX are omitted in the void analysis.

A three-dimensional representation of the glass bead/rubber composite at the initial material state is shown in Figure 5(a). The initial material states are used to verify the repeatability of sample formulation. Specifically, the preparation of specimens free of air bubbles while maintaining homogeneous distributions of particles. One of the geometrical quantities computed is individual phase dimensions. The particle (glass bead) diameters are calculated to be on average 261($\pm\,65$) microns for the standard sample study with a 42% particle volume fraction. The error bars in Figure 5(b) represent the 95.45% bound of confidence of the particles having on average a particle diameter of 261 ($\pm\,65$) microns.

4. Material studies

Using the developed image processing procedure described above, four experimental studies are investigated in order to quantify the amount of microscale damage (i.e. voids) for each sample.

4.1. Effect of particle volume fraction

The first study considers varying the particle (glass bead) volume fraction. Using the image analysis procedures, the particle volume fractions are determined as

follows: $c_p = 0.2221$, $c_p = 0.3242$, and $c_p = 0.4191$ with a mean particle diameter of $d = 261.2$ microns. The standard deviation in volume fraction for three samples is 0.0009, 0.0031, and 0.0098 respectively, which is less than 1% of each mean volume fraction. For simplicity of presentation, volume fractions and the mean particle diameter will be designated as: $c_p = 0.2$, $c_p = 0.3$, $c_p = 0.4$, and $d = 261$ μm. All samples in this study are loaded to 300 N. The resulting loading curves are shown in Figure 6(a) where the horizontal error bars represent the range of displacements seen among the three samples tested. As expected, increasing the particle volume fraction increases the stiffness of the material.

Next, we investigate the macroscopic response by quantifying the amount of damage for each sample. This is done by computing the total volume fraction of the void phase in the relaxed scanned configuration marked in Figure 6(a) by the points **A**, **B**, and **C** (i.e. after 24-hour relaxation). Figure 6(b) shows the void volume fraction as a function of the particle volume fraction. Note that a non-linear like relationship exists between the amount of macroscopic displacement and the number of voids formed as the c_p is increased. Moreover, when increasing the c_p, a greater amount of complexity is added to the system, thus introducing larger spread in the data as seen in Figure 6(b).

To further investigate the interdependence between the volume fraction of particles and voids at the microscopic level, we quantify the amount of individual phases. Table 1 reflects the increasing amount of particles and voids as c_p is increased. Additionally, a data slice is taken at scanning points **A**, **B**, and **C** to further analyze void formation. The data slices encompass $\sim 20\%$ of the cross-section and are taken from a horizontal slice in the middle of each sample (see Figure 7).

Using the data slices, we gain insight into the dependencies between c_p and c_v. We observe that the voids nucleate at the particle-matrix interface. This is
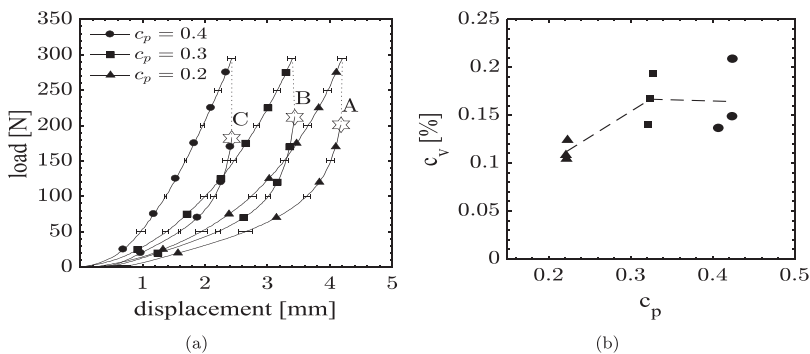

(a) (b)

Figure 6. (a) Higher filled composites show increased stiffness when subjected to uniaxial compression loading. (b) The void volume fraction, c_v, as a function of the particle volume fraction, c_p, at the scanning points marked with stars. Note, a linear fit of the 3 samples is displayed by the dashed line.

Table 1. Comparison of the number of particles N_p (calculated) versus the number of voids N_v (calculated) using the image processing analysis tools for rubber-silica composites with $d = 262\,\mu$m and varied particle volume fraction c_p.

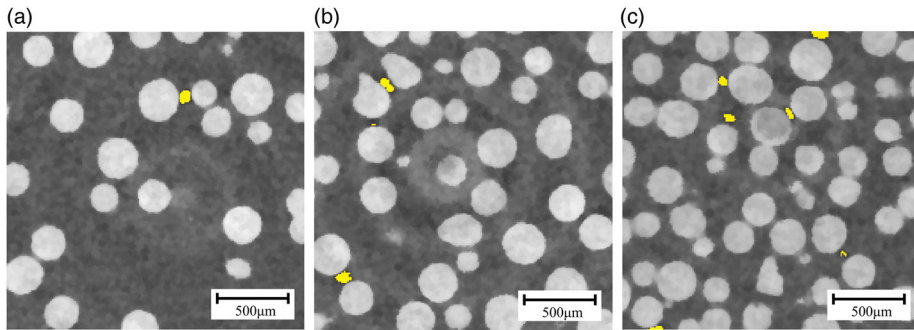| d=261 μm	$c_p = 0.2$	$c_p = 0.3$	$c_p = 0.4$
N_p	18,828	27,241	38,202
N_v	2,862	4,409	4,591

Figure 7. Two-dimensional cross section of composite samples encompassing 20% of surface area of a horizontal slice taken from the middle of the composite samples at scanning points **A**, **B**, and **C** for (a) $c_p = 0.2$, (b) $c_p = 0.3$, and (c) $c_p = 0.4$ depicting the increase of void initiation sites as the c_p is increased. Voids are highlighted in yellow.

consistent with both experimental and computational studies on a variety of systems [66,73–75]. In [66], it was shown that damage nucleation depends on the local stress concentration, but not on the size of the particles. On the other hand, the void growth has a marked size effect (i.e. Most of the failure occurs on large particle interfaces.). Using Table 1 and Figure 7(a), we note that for $c_p = 0.2$ there are fewer initiation sites (particles) for voids to originate. Therefore, there is a significantly lower volume fraction of voids (see Figure 6 (b)). Similarly, the higher volume fraction samples $c_p = 0.3$ and $c_p = 0.4$ contain more particles where voids can initiate and result in higher volume of voids $c_v = 0.17\%$ and $c_v = 0.16\%$, respectively (see Figure 7(b,c)).

Furthermore, we analyze the void characteristics at scans taken at the same points **A**, **B**, and **C**. The associated void size distribution for each volume fraction is shown in Figure 8 in the form of a discrete probability density function (pdf). We observe a larger number of small voids ($\sim$50 μm) in the lower filled composite $c_p = 0.2$ shown in Figure 8(a). The mean void size is similar between $c_p = 0.2$ and $c_p = 0.3$ composites. However, in the composite with $c_p = 0.3$, a smaller inter-particle spacing exists compared to $c_p = 0.2$ (see Figure 7(b)). We conclude that the voids that are created are able to grow in the softer matrix. Thus, the possibility of voids coming into contact with one another is increased. Two or more existing voids may coalesce which, increases the volume of the voids. Therefore, as c_p increases the voids become larger in size thus the enhanced tail to the right in the distributions. Note however that the highest filled composite $c_p = 0.4$
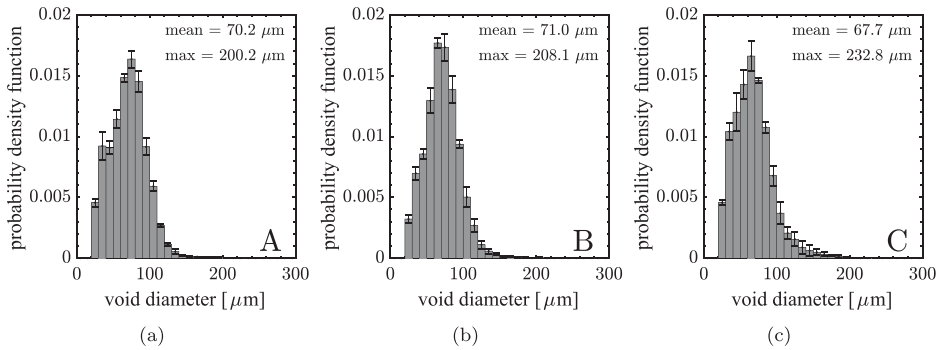
Figure 8. Distribution of void size diameters in the compressed rubber-silica composites with varied particle volume fraction (a) $c_p = 0.2$, (b) $c_p = 0.3$, and (c) $c_p = 0.4$. Although the mean void size is similar between all samples, the voids are larger in size as c_p is increased. This is indicated by the enhanced tail in the distribution to the right. The error bars represent ($\pm 2\sigma$) from the mean.

contains 40% more particles (lower inter-particle spacing Figure 7(c)) and therefore does not allow the existing voids to continue growing freely. Thereby, restricting the growth/size of the voids. This composite contains a larger amount of smaller voids and thus the total volume fraction is comparable to that of $c_p = 0.3$ (see Figure 6(b)). Moreover, the large number of smaller particles is harder to detect and analyze. This leads to large uncertainty in the data (i.e. higher spread of data points in Figure 6(b)). These observations help explain why the higher filled composites contain similar volume fraction of voids despite having different material bulk responses.

4.2. Effect of particle diameter

In this study the particle diameter, d, is varied. The mean particle diameters are determined as follows: $d = 157.5(\pm 45)\,\mu$m, $d = 261.2(\pm 65)\,\mu$m, and $d = 350.9(\pm 104)\,\mu$m on average. Where the ($\pm 2\sigma$) represents the 95.45% bound of confidence of the particles having on average a particle diameter of ($\pm 2\sigma$) microns for each set. The particle volume fraction is kept approximately constant, and calculated for each set as $c_p = 0.4168$, $c_p = 0.4191$, $c_p = 0.4311$ and will be denoted as $c_p = 0.4$. The standard deviation in volume fraction for all of these scans is 0.0230, 0.0098, and 0.0029 respectively. The particle diameter will be denoted as: $d = 158\,\mu$m, $d = 261\,\mu$m, and $d = 351\,\mu$m. In this study, the composite samples with $d = 158\,\mu$m are tomographically scanned at a higher resolution of 5.41 μm/pixel in order to capture the smaller details (glass beads). Due to the extensive acquisition time, this is the only set scanned at this resolution. The averaged force-displacement curves in Figure 9 (a) indicate a negligible particle size effect in the rubber-silica composite, especially in the early loading stage. Moreover, the curves fall within the

statistical error. This is a typical result for micron size particles, where the size effect has a negligible role on the macroscopic properties (e.g. Young's modulus) [76].

Interestingly, there is an effect on the amount of voids created as a function of the particle size (see Figure 9(b)). A vertical two-dimensional slice is taken from the middle of the composites with $d = 261$ μm, and $d = 351$ μm presented in Figure 10(a,b), respectively. The images are taken from the scans marked by **D** in Figure 9(a). The data slices are used to understand the non-monotonic like behaviour of the void content. The image slice in Figure 10(b) shows a significant reduction in inter-particle spacing (i.e. for larger particles). A result due to the larger particle diameter $d = 351$ μm necessary to reach the same 40% volume fraction of particles. Therefore, particles are in closer contact when compared to the $d = 261$ μm system. As mentioned previously, voids are created at the particle-matrix interface. In the $d = 351$ μm system, particles form chain-like clusters that reduce the stress concentrations in the composite. This chain formation leads to a reduced number of void initiation sites. On the other hand, the particle distance of free (not chained) particles is a driving mechanism for stress concentrations that promote debonding.

To further investigate the physics occurring in this study, the void size distributions Figure 11 are computed. In composites with $d = 158$ μm, higher resolutions scans allow us to capture a large amount of small voids (see Figure 11(a)). This is due to the large amount of particles (i.e. void initiation sites) used to achieve $c_p = 0.4$. The larger amount of particles, however, inhibit the growth of those voids since the inter-particle spacing is decreased substantially. This leads to a more one-sided distribution in Figure 11(a). As discussed previously, the standard composite with $d = 261$ μm contains a particular amount of particles where voids that nucleate and are able to grow (see Figure 10(a)). In this composite (i.e. $d = 261$ μm) the peak in the distribution indicates there
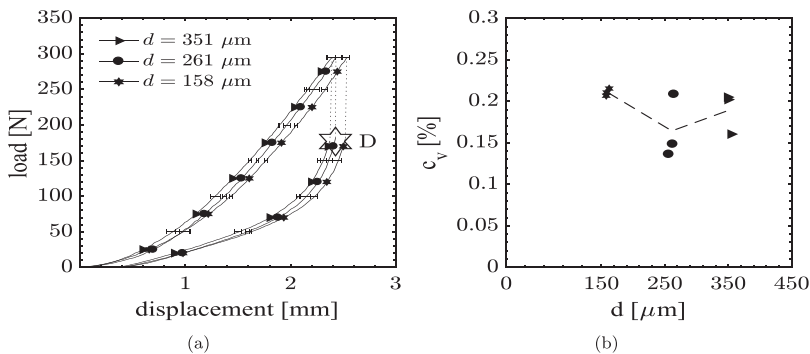

Figure 9. (a) A negligible size effect on stiffness is seen when varying the particle diameter, d, when the composites are subjected to uniaxial compression loading and (b) the mean void volume fraction as a function of the mean d. Dashed line represents the linear fit of corresponding testing data (3 samples).
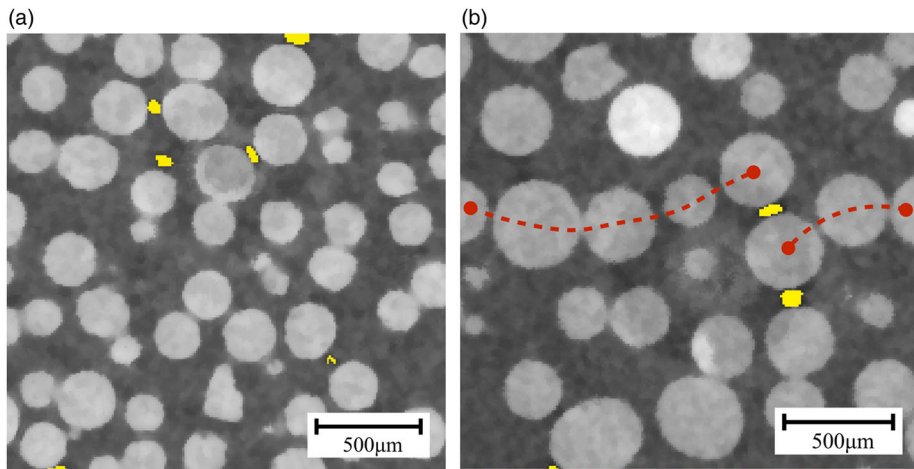
Figure 10. (a) Lateral view two-dimensional slice of composite sample of $c_p = 0.4$ with $d = 261\,\mu m$ and (b) $c_p = 0.4$ with $d = 351\,\mu m$. Voids are marked in yellow, and particle chains are highlighted by red dashed lines.

is a dominant void size favourable in the onset of damage Figure 11(b). Additionally, this system has a Gaussian-like void size distribution. In comparison, the composites with $d = 351\,\mu m$, voids are created and able to grow in an alternative way. Two or more voids have a higher possibility of coming in contact with one another and become one larger void. A result of the reduced inter-particle spacing and more frequent particle chaining in this composite spreads and flattens the distribution peak. The plateau in the void size distribution for $d = 351\,\mu m$ in Figure 11(c) indicates there is a range of void sizes that are preferential. Therefore, the larger void content is attributed to the larger size of the voids and not the amount of voids contained. These observations help explain the non-monotonic like trend in the void volume fraction as a function of particle size diameter.
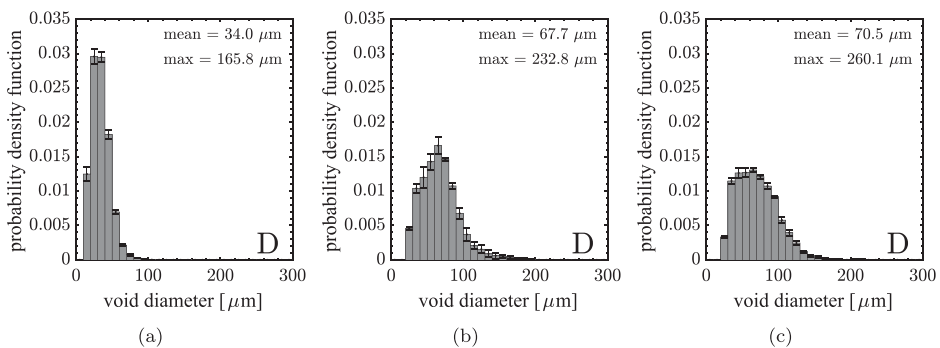

Figure 11. Void size distribution of compressed rubber-silica composites with particle diameter: (a) $d = 158\,\mu m$ shows a large amount of small voids by the left-sided distribution, (b) $d = 261\,\mu m$ shows a Gaussian like distribution, and (c) $d = 351\,\mu m$ shows a range of void sizes that are preferable to void growth by the plateau in the distribution.

4.3. Local damage phenomena and its evolution

In this study, standard samples of $c_p = 0.4$ and $d = 261\,\mu m$ are subjected to incremental loading. Incremental loading allows for the understanding of void evolution which, is the only damage mechanism considered in this study. The composite sample is compressed to a predefined load of $100\,N$ scanned after the relaxation period and then loaded again incrementally by $100\,N$ until reaching $400\,N$. Note, State 1 corresponds to a compressed load of $100\,N$, State 2–200 N, State 3–300 N, and lastly State 4–400 N. The resulting loading profile for this incremental loading and scanning study is shown in Figure 12(a). The amount of voids as a function of the loading state is depicted in Figure 12(b). The initial void free unloaded State 0 is verified. There are almost no voids present until the sample reaches a load of $200\,N$. Then the voids rapidly nucleate and grow in regions of stress concentrations. A similar trend has been shown in [66,77].

In order to understand how these voids nucleate and grow, the associated void size distributions for each loading state are shown in Figure 13. These distributions are acquired from the scans taken after each relaxation period and marked **I**, **II**, **III**, and **IV**. The void size distribution in Figure 13(a) reveals there is a large number of voids created that remain fairly small under the given load. As the load is incremented, from one compression state to the next, the void size distribution shifts towards the right indicating the voids that were created in the initial compression have grown in size. After the initial compression, the distribution of void sizes becomes levelled (see Figure 13(b)). This highlights the void growth. At the $300\,N$ load level, the mean void size of ~$66\,\mu m$ emerges and the void distribution becomes close to Gaussian. In the final stages of loading (i.e. $400\,N$), the distribution shifts to the right demonstrating an increase in both the mean and maximum void size.

To further analyze void nucleation and growth phenomena, data slices are taken at scanning points **II**, **III**, and **IV**. The data slices encompass $\sim 20\%$ of
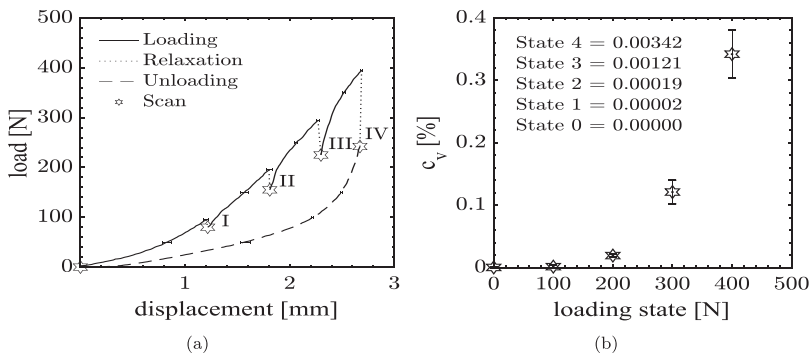

Figure 12. (a) Loading vs. displacement curves for incremental compression of the standard rubber-silica composite and (b) volume of voids c_v increases significantly once the load has reached $200\,N$.
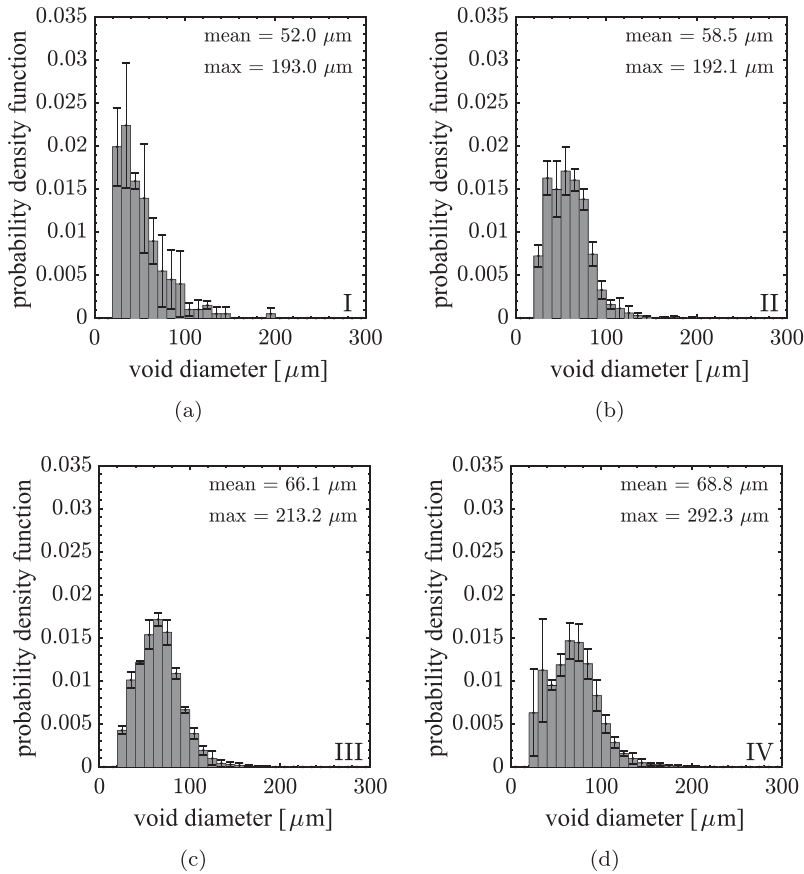
Figure 13. Void size distribution for different loading states: (a) State-1 shows a very one-sided distribution, (b) in State-2 a rapid transition shows growth, (c) State-3 shows the mean void structure is forming, and (d) in State-4 voids grow in size and the distributions broadens.

the cross-section and are taken from a horizontal slice in the middle of each sample (see Figure 14). In the second loading state (i.e. 200 N load level) voids nucleate at the particle matrix interface. As the load is increased to state III and IV, the existing voids grow in size, coalesce, and other void initiation sites are created.

4.4. Effect of surface treatments on bonding characteristics

In this study, we investigate the surface effects. We coat the silica glass beads with a solution used to promote interface bonding, Silane, and a solution used to demote bonding, Pol-Ease release agent. This study is used to assess the weak and strong bonding regimes. A small increase in mechanical stiffness is seen in composites with Silane surface treated particles (see Figure 15). The releasing agent, on the other hand, significantly changes the mechanical stiffness of the composite. This composite deforms ~55% reaching a load of 55 N only. Note
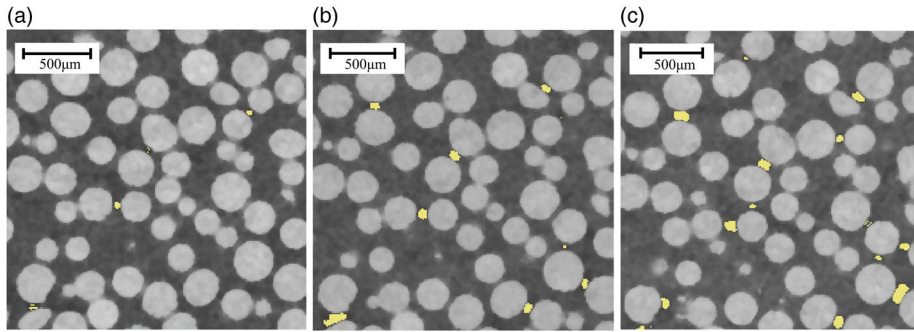
Figure 14. Two-dimensional cross section of composite samples encompassing 20% of surface area of a horizontal slice taken from the middle of the composite samples at scanning points (a) **II**, (b) **III**, and (c) **IV** depicting the void nucleation and growth as the load is incremented. Voids are highlighted in yellow.
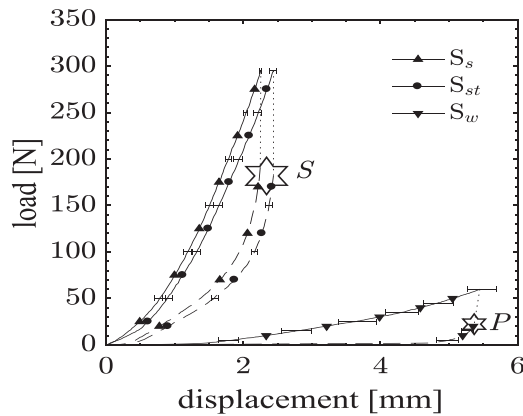

Figure 15. Coating the surface of the particulates with Silane, (S_s), does not change the mechanical response considerably when compared to the standard sample, (S_{st}). Alternatively, coating the surface with the releasing agent, (S_w), significantly reduces the stiffness.

that the strong bonding study is denoted by S_s, the untreated composite (standard sample) is denoted with S_{st}, and weak bonding is denoted by S_w.

The void distributions are taken at the compressed states denoted with the letters **S** and **P** for S_{st} and S_s, and S_w particles, respectively (see Figure 16). The void size distribution between the untreated S_{st} and the S_s treated composite show little distinction. The mean void size for silane treated composites decreases slightly. Moreover, the maximum void size increases. On the other hand, Pol-Ease treated composites show a significant increase in void size where voids reach up to 1328.42 μm on average. This can be attributed to the weak bonding between the particle and matrix. The low bonding strength at the interface allows the silica particles to be liberated from the matrix easily. Voids thus nucleate easier in this weakly bonded composite and grow
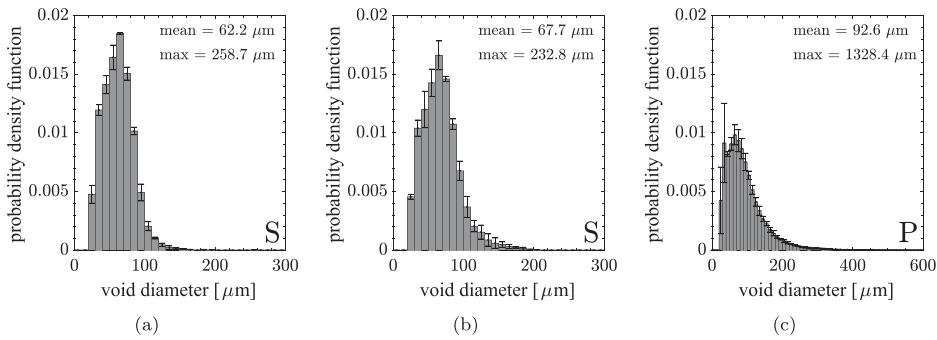
Figure 16. Void size distribution of compressed rubber-silica composites with surface treated silica glass beads (a) Silane treated, (b) standard non-treated, and (c) release agent treated shows significant increase in void sizes in weakly bonded composites

substantially due to the overall decreased stiffness. Therefore, the composite's response to loading is similar to that of the pure rubber (see Figure 2).

5. Conclusions

In this work, we present an image-based materials testing approach using micro-computed tomography to observe void formation and its evolution while varying the microstructure of rubber-glass bead composites. A material testing methodology is developed resulting in precise and reliable force-displacement data using the *in situ* material testing stage.

Visualization and analysis software is used to determine multiscale coupling between the morphological and mechanical response of the composites when subjected to uniaxial compression loading. Microstructure-statistics-property relations are established. We test multiple samples to ensure repeatability and use large data sets for the statistical calculations representing the amount of microscale damage. The developed image processing pipeline accurately identifies particles and voids which are critical for material response assessment.

The investigation of varied microstructure's effects on microscale damage can be summarised as follows. When varying the particle volume fraction, the void growth saturates with higher filled composites despite having different material bulk responses to loading. When varying the particle diameter a non-monotonic like trend in void content is observed, a result of chain-like clusters that reduce stress concentrations in the largest particle diameter composite. When studying void evolution, highly nonlinear void growth is observed with each incremental loading step. Lastly, comparisons of strong and weak bonding agents used for particle matrix interfacial bonding results in $5\times$ increases in void sizes.

In addition to the fundamental understanding, these experiments serve as validation data sets for multiscale modelling approaches. The constitutive model development, validation, and co-designed simulations and experiments are a natural next step. This analysis and framework yields new insight of

particulate composite materials required for optimal material design. Furthermore, the novel, thorough, and reliable experimental and image processing pipelines are applicable to other material systems.

Disclosure statement

The authors have no competing interests.

References

[1] T. Monetta, A. Acquesta, and F. Bellucci, Graphene/epoxy coating as multifunctional material for aircraft structures, Aerospace 2 (2015), pp. 423–434.

[2] H. Qi, B. Schulz, T. Vad, J. Liu, E. Mäder, G. Seide, and T. Gries, Novel carbon nanotube/cellulose composite fibers as multifunctional materials, ACS Appl. Mat. Int. 7 (2015), pp. 22404–22412.

[3] C.F. Matos, F. Galembeck, and A.J. Zarbin, Multifunctional materials based on iron/iron oxide-filled carbon nanotubes/natural rubber composites, Carbon 50 (2012), pp. 4685–4695.

[4] S. Kumar, S. Raj, S. Jain, and K. Chatterjee, Multifunctional biodegradable polymer nanocomposite incorporating graphene-silver hybrid for biomedical applications, Mater. Des. 108 (2016), pp. 319–332.

[5] J. Oden, T. Belytschko, J. Fish, T. Hughes, C. Johnson, D. Keyes, A. Laub, L. Petzold, D. Srolovitz, and S. Yip, Simulation-based engineering science: Revolutionizing engineering science through simulation, Tech. Rep., 2006.

[6] K. Matouš, M.G. Geers, V.G. Kouznetsova, and A. Gillman, A review of predictive nonlinear theories for multiscale modeling of heterogeneous materials, J. Comput. Phys. 330 (2017), pp. 192–220.

[7] G.B. Olson, Computational design of hierarchically structured materials, Science 277 (1997), pp. 1237–1242.

[8] N.R. Council, Integrated Computational Materials Engineering: A Transformational Discipline for Improved Competitiveness and National Security, National Academies Press, Washington, DC, 2008.

[9] D.L. McDowell, J. Panchal, H.J. Choi, C. Seepersad, J. Allen, and F. Mistree, Integrated Design of Multiscale, Multifunctional Materials and Products, Butterworth-Heinemann, Burlington, MA, 2009.

[10] M.J. Beran and A. Pytte, Statistical continuum theories, *Amer. J. Phys.* 36 (1968), pp. 923–923.

[11] D. McDowell, S. Ghosh, and S. Kalidindi, Representation and computational structure-property relations of random media, *JOM* 63 (2011), pp. 45–51.

[12] S. Torquato, Random Heterogeneous Materials: Microstructure and Macroscopic Properties, Vol. 16, Springer Science & Business Media, Princeton, NJ, 2013.

[13] H. Lee, M. Brandyberry, A. Tudor, and K. Matouš, Three-dimensional reconstruction of statistically optimal unit cells of polydisperse particulate composites from microtomography, *Phys. Rev. E* 80 (2009), pp. 061301.

[14] A. Gillman, K. Matouš, and S. Atkinson, Microstructure-statistics-property relations of anisotropic polydisperse particulate composites using tomography, *Phys. Rev. E* 87 (2013), pp. 022208.

[15] J. Zangenberg and P. Brøndsted, Quantitative study on the statistical properties of fibre architecture of genuine and numerical composite microstructures, *Compos. A, Appl. Sci. Manuf.* 47 (2013), pp. 124–134.

[16] R. Young, E. Kirk, D. Williams, and H. Ahmed, Fabrication of planar and cross-sectional TEM specimens using a focused ion beam, *MRS Proc.* 199 (1990), pp. 205.

[17] D.P. Basile, R. Boylan, B. Baker, D. Soza, and K. Hayes, Fibxtem – focussed ion beam milling for TEM sample preparation. *MRS Proc.* 254 (1991), pp. 23–41.

[18] R. Wirth, Focused Ion Beam (FIB) combined with SEM and TEM: Advanced analytical tools for studies of chemical composition, microstructure and crystal structure in geomaterials on a nanometre scale, *Chem. Geol.* 261 (2009), pp. 217–229.

[19] K. Benzerara, N. Menguy, F. Guyot, C. Vanni, and P. Gillet, TEM study of a silicate-carbonate-microbe interface prepared by focused ion beam milling, *Geochim. Cosmochim. Acta* 69 (2005), pp. 1413–1422.

[20] J. Li, M. Elmadagli, V. Gertsman, J. Lo, and A. Alpas, FIB and TEM characterization of subsurfaces of an Al–Si alloy (a390) subjected to sliding wear, *Mater. Sci. Eng. A* 421 (2006), pp. 317–327.

[21] L. Holzer, F. Indutnyi, P. Gasser, B. Münch, and M. Wegmann, Three-dimensional analysis of porous BaTiO3 ceramics using FIB nanotomography, *J. Microsc.* 216 (2004), pp. 84–95.

[22] R. Wirth, Focused Ion Beam (FIB) a novel technology for advanced application of micro-and nanoanalysis in geosciences and applied mineralogy, *Eur. J. Mineral.* 16 (2004), pp. 863–876.

[23] A. Gillman, M. Roelofs, K. Matouš, V. Kouznetsova, O. van der Sluis, and M. van Maris, Microstructure statistics–property relations of silver particle-based interconnects, *Mater. Des.* 118 (2017), pp. 304–313.

[24] D. Yushu, S. Lee, and K. Matouš, Sharp volumetric billboard based characterization and modeling of complex 3D Ni/Al high energy ball milled composites, *Mech. Mater.* 108 (2017), pp. 93–106.

[25] V. Kuperman, Magnetic Resonance Imaging: Physical Principles and Applications, Academic Press, San Diego, CA, 2000.

[26] B.P. Flannery, H.W. Deckman, W.G. Roberge, and K.L. D'AMICO, Three-dimensional X-ray microtomography, *Science* 237 (1987), pp. 1439–1444.

[27] J. Kinney, Q. Johnson, U. Bonse, M. Nichols, R. Saroyan, R. Nusshardt, R. Pahl, and J. Brase, Three dimensional X-ray computed tomography in materials science, *MRS Bull.* 13 (1988), pp. 13–18.

[28] J. Kinney, M. Nichols, U. Bonse, S. Stock, T. Breunig, A. Guvenilir, and R. Saroyan, Nondestructive imaging of materials microstructures using X-ray tomographic microscopy, *MRS Online Proc. Libr. Arch.* 217 (1990), pp. 81–95.

[29] P. Rüegsegger and B. Köller, *A micro-CT system for the nondestructive analysis of bone samples*, 10th International Bone Densitometry Workshop, Venice, Italy, 1994.

[30] E.L. Ritman, Micro-computed tomography current status and developments, *Annu. Rev. Biomed. Eng.* 6 (2004), pp. 185–208.

[31] S. Stock, X-ray microtomography of materials, *Int. Mater. Rev.* 44 (1999), pp. 141–164.

[32] G. Wang, H. Yu, and B. De Man, An outlook on X-ray CT research and development, *Med. Phys.* 35 (2008), pp. 1051–1064.

[33] B.M. Patterson and C.E. Hamilton, Dimensional standard for micro X-ray computed tomography, *Anal. Chem.* 82 (2010), pp. 8537–8543.

[34] S. Gallier and F. Hiernard, Microstructure of composite propellants using simulated packings and X-ray tomography, *J. Propuls. Power* 24 (2008), pp. 154–157.

[35] B.M. Patterson, J.P. Escobedo-Diaz, D. Dennis-Koller, and E. Cerreta, Dimensional quantification of embedded voids or objects in three dimensions using X-ray tomography, *Microsc. Microanal.* 18 (2012), pp. 390–398.

[36] T. Dillard, F. Nguyen, E. Maire, L. Salvo, S. Forest, Y. Bienvenu, J.D. Bartout, M. Croset, R. Dendievel, and P. Cloetens, 3D quantitative image analysis of open-cell nickel foams under tension and compression loading using X-ray microtomography, *Philos. Mag.* 85 (2005), pp. 2147–2175.

[37] Q. Zhang, H. Toda, Y. Takami, Y. Suzuki, K. Uesugi, and M. Kobayashi, Assessment of 3d inhomogeneous microstructure of highly alloyed aluminium foam via dual energy k-edge subtraction imaging, *Philos. Mag.* 90 (2010), pp. 1853–1871.

[38] T. Ohgaki, H. Toda, M. Kobayashi, K. Uesugi, M. Niinomi, T. Akahori, T. Kobayash, K. Makii, and Y. Aruga, In situ observations of compressive behaviour of aluminium foams by local tomography using high-resolution X-rays, *Philos. Mag.* 86 (2006), pp. 4417–4438.

[39] G.N. Hounsfield, Computerized transverse axial scanning (tomography): Part 1. description of system, *Br. J. Radiol.* 46 (1973), pp. 1016–1022.

[40] B. London, R.N. Yancey, and J. Smith, High-resolution X-ray computed tomography of composite materials, *Mater. Eval.* 48 (1990), pp. 604–608.

[41] G.Y. Baaklini, R.T. Bhatt, A.J. Eckel, P. Engler, R.W. Rauser, and M.G. Castelli, X-ray microtomography of ceramic and metal matrix composites, *Mater. Eval.* 53 (1995), pp. 1040–1044.

[42] D. Bull, S. Spearing, and I. Sinclair, Observations of damage development from compression-after-impact experiments using ex situ micro-focus computed tomography, *Compos. Sci. Technol.* 97 (2014), pp. 106–114.

[43] M. Barburski, I. Straumit, X. Zhang, M. Wevers, and S.V. Lomov, Micro-ct analysis of internal structure of sheared textile composite reinforcement, *Compos. A, Appl. Sci. Manuf.* 73 (2015), pp. 45–54.

[44] A. Guvenilir, T. Breunig, J. Kinney, and S. Stock, Direct observation of crack opening as a function of applied load in the interior of a notched tensile sample of Al-Li 2090, *Acta Mater.* 45 (1997), pp. 1977–1987.

[45] S. Youssef, E. Maire, and R. Gaertner, Finite element modelling of the actual structure of cellular materials determined by X-ray tomography, *Acta Mater.* 53 (2005), pp. 719–730.

[46] K. Madi, S. Forest, M. Boussuge, S. Gailliègue, E. Lataste, J.Y. Buffière, D. Bernard, and D. Jeulin, Finite element simulations of the deformation of fused-cast refractories based on X-ray computed tomography, *Comput. Mater. Sci.* 39 (2007), pp. 224–229.

[47] O. Caty, E. Maire, S. Youssef, and R. Bouchet, Modeling the properties of closed-cell cellular materials from tomography images using finite shell elements, *Acta Mater.* 56 (2008), pp. 5524–5534.

[48] J.Y. Buffière, P. Cloetens, W. Ludwig, E. Maire, and L. Salvo, In situ X-ray tomography studies of microstructural evolution combined with 3d modeling, *MRS Bull.* 33 (2008), pp. 611–619.

[49] A. Somashekar, S. Bickerton, and D. Bhattacharyya, Compression deformation of a biaxial stitched glass fibre reinforcement: Visualisation and image analysis using X-ray micro-CT, *Compos. A, Appl. Sci. Manuf.* 42 (2011), pp. 140–150.

[50] M.B. Bettaieb, X. Lemoine, O. Bouaziz, A.M. Habraken, and L. Duchêne, Numerical modeling of damage evolution of DP steels on the basis of X-ray tomography measurements, *Mech. Mater.* 43 (2011), pp. 139–156.

[51] R. Sencu, Z. Yang, Y. Wang, P. Withers, C. Rau, A. Parson, and C. Soutis, Generation of micro-scale finite element models from synchrotron X-ray CT images for multidirectional carbon fibre reinforced composites, *Compos. A, Appl. Sci. Manuf.* 91 (2016), pp. 85–95.

[52] T.T. Nguyen, J. Yvonnet, M. Bornert, and C. Chateau, Initiation and propagation of complex 3d networks of cracks in heterogeneous quasi-brittle materials: Direct comparison between in situ testing-microCT experiments and phase field simulations, *J. Mech. Phys. Solids.* 95 (2016), pp. 320–350.

[53] Y. Tsang and C. Tsang, A particle-tracking method for advective transport in fractures with diffusion into finite matrix blocks, *Water. Resour. Res.* 37 (2001), pp. 831–835.

[54] A. Germaneau, P. Doumalin, and J.C. Dupré, Comparison between X-ray micro-computed tomography and optical scanning tomography for full 3D strain measurement by digital volume correlation, *NDT E Int.* 41 (2008), pp. 407–415.

[55] S.F. Nielsen, H.F. Poulsen, F. Beckmann, C. Thorning, and J. Wert, Measurements of plastic displacement gradient components in three dimensions using marker particles and synchrotron X-ray absorption microtomography, *Acta Mater.* 51 (2003), pp. 2407–2415.

[56] A. Germaneau, P. Doumalin, and J.C. Dupré, 3D strain field measurement by correlation of volume images using scattered light: Recording of images and choice of marks, *Strain* 43 (2007), pp. 207–218.

[57] K. Haldrup, S.F. Nielsen, and J.A. Wert, A general methodology for full-field plastic strain measurements using X-ray absorption tomography and internal markers, *Exp. Mech.* 48 (2008), pp. 199–211.

[58] Y. Barranger, P. Doumalin, J.C. Dupre, A. Germaneau, S. Hedan, and V. Valle, Evaluation of three-dimensional and two-dimensional full displacement fields of a single edge notch fracture mechanics specimen, in light of experimental data using X-ray tomography, *Eng. Fract. Mech.* 76 (2009), pp. 2371–2383.

[59] B. Wang, B. Pan, and G. Lubineau, Morphological evolution and internal strain mapping of pomelo peel using X-ray computed tomography and digital volume correlation, *Mater. Des.* 137 (2018), pp. 305–315.

[60] E. Ferrié, J.Y. Buffière, W. Ludwig, A. Gravouil, and L. Edwards, Fatigue crack propagation: In situ visualization using X-ray microtomography and 3D simulation using the extended finite element method, *Acta Mater.* 54 (2006), pp. 1111–1122.

[61] S. Birosca, J. Buffiere, F. Garcia-Pastor, M. Karadge, L. Babout, and M. Preuss, Three-dimensional characterization of fatigue cracks in Ti-6246 using X-ray tomography and electron backscatter diffraction, *Acta Mater.* 57 (2009), pp. 5834–5847.

[62] S. Terzi, L. Salvo, M. Suéry, N. Limodin, J. Adrien, E. Maire, Y. Pannier, M. Bornert, D. Bernard, M. Felberbaum, et al. In situ X-ray tomography observation of inhomogeneous deformation in semi-solid aluminium alloys, *Scr. Mater.* 61 (2009), pp. 449–452.

[63] S.H. Ibrahim, M. Neumann, F. Klingner, V. Schmidt, and T. Wejrzanowski, Analysis of the 3d microstructure of tape-cast open-porous materials via a combination of experiments and modeling, *Mater. Des.* 133 (2017), pp. 216–223.

[64] H. Lee, A.S. Gillman, and K. Matouš, Computing overall elastic constants of polydisperse particulate composites from microtomographic data, *J. Mech. Phys. Solids* 59 (2011), pp. 1838–1857.

[65] A. Gillman and K. Matouš, Third-order model of thermal conductivity for random polydisperse particulate materials using well-resolved statistical descriptions from tomography, *Phys. Lett. A* 378 (2014), pp. 3070–3073.

[66] K. Matouš, H. Inglis, X. Gu, D. Rypl, T. Jackson, and P.H. Geubelle, Multiscale modeling of solid propellants: From particle packing to failure, *Compos. Sci. Technol.* 67 (2007), pp. 1694–1708.

[67] T.L. Jackson, Modeling of heterogeneous propellant combustion: A survey, *AIAA J.* 50 (2012), pp. 993–1006.

[68] H. Berghout, S. Son, C. Skidmore, D. Idar, and B. Asay, Combustion of damaged PBX 9501 explosive, *Thermochim. Acta* 384 (2002), pp. 261–277.

[69] T.M. Willey, L. Lauderbach, F. Gagliardi, T. van Buuren, E.A. Glascoe, J.W. Tringe, J.R. Lee, H.K. Springer, and J. Ilavsky, Mesoscale evolution of voids and microstructural changes in hmx-based explosives during heating through the β-δ phase transition, *J. Appl. Phys.* 118 (2015), pp. 055901.

[70] *BOSE ElectroForce Fatigue Test Instruments*. Available at http://www.devicetesting.com/tools_elf3200.cfm.

[71] *FEI, Amira-Avizo 3D Software*. Available at https://www.fei.com/software/amira-avizo/.

[72] *Bruker. MicroCT, Skycan: High Resolution Desk-Top Micro-CT*. Available at http://bruker-microct.com/products/1172.htm.

[73] S. Nutt and A. Needleman, Void nucleation at fiber ends in Al-SiC composites, *Scr. Metal.* 21 (1987), pp. 705–710.

[74] D. Hull and D. Rimmer, The growth of grain-boundary voids under stress, *Philos. Mag.* 4 (1959), pp. 673–687.

[75] D. Lloyd, Aspects of fracture in particulate reinforced metal matrix composites, *Acta Metall. Mater.* 39 (1991), pp. 59–71.

[76] S.Y. Fu, X.Q. Feng, B. Lauke, and Y.W. Mai, Effects of particle size, particle/matrix interface adhesion and particle loading on mechanical properties of particulate–polymer composites, *Compos. B, Eng.* 39 (2008), pp. 933–961.

[77] K. Matouš and P.H. Geubelle, Multiscale modelling of particle debonding in reinforced elastomers subjected to finite deformations, *Internat. J. Numer. Methods Engrg.* 65 (2006), pp. 190–223.